

Group Equivariant Generative Adversarial Networks

Neel Dey^{1*}, Antong Chen², and Soheil Ghafurian²

¹ Computer Science & Engineering, New York University, NY, USA
neel.dey@nyu.edu

² Merck & Co., Inc., Kenilworth, NJ, USA
{antong.chen, soheil.ghafurian}@merck.com

Abstract. Generative adversarial networks are the state of the art for generative modeling in vision, yet are notoriously unstable in practice. This instability is further exacerbated with limited training data. However, in the synthesis of domains such as medical or satellite imaging, it is often overlooked that the image label is invariant to global image symmetries (e.g., rotations and reflections). In this work, we improve gradient feedback between generator and discriminator using an inductive symmetry prior via group-equivariant convolutional networks. We replace convolutional layers with equivalent group-convolutional layers in both generator and discriminator, allowing for better optimization steps and increased expressive power with limited samples. In the process, we extend recent GAN developments to the group-equivariant setting. We demonstrate the utility of our methods by improving both sample fidelity and diversity in the class-conditional synthesis of a diverse set of globally-symmetric imaging modalities.

1 Introduction

Generative visual modeling is an area of active research, time and again finding diverse and creative applications. A prevailing approach is the generative adversarial network (GAN), wherein density estimation is implicitly approximated by a min-max game between two neural networks [19]. Recent GANs are capable of high-quality natural image synthesis and scale dramatically with increases in batch size and data availability [9]. However, GANs are prone to instability due to the difficulty of achieving a local equilibrium between the two networks.

Frequent GAN failures include one or both networks diverging or the generator only capturing a few modes of the empirical distribution. Several methods have been proposed to alleviate this instability including modifying training objectives [2, 28], hierarchical methods [29], latent optimization [63], and strongly regularizing one or both networks [20, 41, 65, 18], among others. In practice, one or all of the above techniques are ultimately adapted to specific use cases.

A commonality between these works is the usage of large-scale image datasets – ranging from hundreds of thousands [38] to millions [51] of samples. This

* Work done while interning at Merck & Co., Inc., Rahway, NJ, USA.

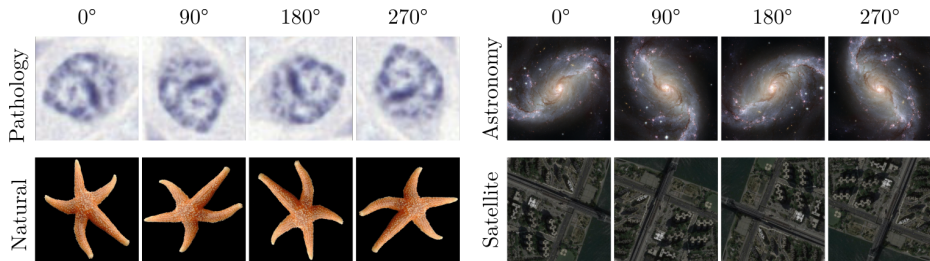


Fig. 1. Several image modalities have no preferred orientation for tasks such as classification. We improve their generative visual modeling by utilizing global image symmetries within a GAN framework. Image credits: [13, 4, 22, 25].

precludes the direct application of GANs to domains with limited samples, as smaller datasets empirically lead to training collapse more often. Sample complexity concerns are highly relevant in fields such as medical imaging, where annotation for conditional image synthesis [40] may be scarce due to either the effort involved or the domain expertise required.

GANs ubiquitously use convolutional layers which exploit the approximate translation invariance and equivariance of image labels and distributions, respectively. Unfortunately, other inherent symmetries such as rotations and reflections are not accounted for by standard convolutional layers. However, a group-theoretic redefinition of the convolutional layer can account for roto-reflective transformations [14], and improve baseline image classification [58] and segmentation [36, 11]. This reformulation implicitly respects an underlying geometry of the data and increases sample efficiency significantly [62].

In this work, we improve the generative modeling of images with transformation invariant labels by using an inductive bias of symmetry. We replace all convolutions with group-convolutions and thus reduce the sample complexity of both networks, thereby extending GANs to the small data regime. As a consequence, gradient feedback between the two networks is improved. To our knowledge, we are the first to introduce group equivariance to GANs and use geometric considerations in both generator and discriminator. Further, we show that recent insights in improving GAN training are fully compatible with group-equivariance with careful reformulations. Our contributions are as follows,

1. We introduce a symmetry prior via group-equivariant convolutions in the generative adversarial framework.
2. We improve class-conditional image synthesis in terms of sample fidelity and diversity across various imaging modalities with limited data.

2 Related work

Equivariant CNNs. Equivariance to geometric transformations is key to understanding image representations within a convolutional network [34, 5]. Cohen

& Welling [14] proposed a generalization of convolutional layers called group-convolutions which in addition to translation, exploit rotation and reflection. Group-convolutions possess a higher degree of weight sharing and decrease sample complexity. This has since been extended to other symmetries on both finite and continuous groups. See [15] for a formal treatment of equivariant CNNs.

Geometric Discriminators. Geometric considerations in GANs have largely focused on the discriminator. Chen, et al. [10] propose a multi-task discriminator which additionally predicts the degree by which an input image has been rotated. Without this rotation loss, the discriminator may only need to retain representations that it can use to distinguish real and fake, not representations that can provide better critique to the generator. Our work uses rotation-equivariant representations explicitly without needing auxiliary rotation losses.

Given a formalization of equivariant CNNs, capsule networks [23, 52] naturally arise. Preliminary work has shown that using a capsule network for the discriminator [27, 57] improves synthesis on toy datasets. However, capsule networks require complex training strategies, restrict architectural choices, and may not be compatible with recent insights in GAN training. Our work integrates seamlessly with existing techniques and scales to higher resolutions.

Geometric Generators. Emerging work has examined the use of geometric approaches in the generator. ST-GANs [35] use a spatial transformer network [26] to generate realistic deformations of a foreground object when added to a scene. GAGAN [56] conditions the generator using a statistical shape model to disentangle geometry and appearance towards more realistic deformation of foreground objects. Our proposed generator does not require a shape parameterization and is freely applicable to more diverse image types. A U-Net inspired [50] capsule generator architecture for supervised image-to-image translation was proposed in [3].

GAN sample complexity. More recent work addresses the application of GANs to small data. Wang, et al. [59] demonstrate transfer learning with GANs using pre-trained networks as initializations for generation with a few thousand to tens of thousands of images in the target dataset. Noguchi, et al. [43] generate images from only tens of training examples by fine-tuning batch normalization statistics within a pre-trained generator [9]. We differ from fine-tuning approaches by considering the problem of training *tabula rasa* on higher resolutions with limited data which possess global symmetries.

3 Methods

3.1 Preliminaries

Groups and group-convolutions. A group is a set with an endowed binary function satisfying the properties of closure, associativity, identity, and invert-

ibility. Of relevance, a two-dimensional symmetry group is the set of all transformations under which a geometric object is invariant with an endowed operation of composition. Equivariance to a finite symmetry group can be achieved by either transforming filters [14] or feature maps [17].

Our work utilizes the finite groups $p4$ and $p4m$, which correspond to 90-degree rotations (4 symmetries) and 90-degree rotations and reflections (8 symmetries), respectively. Following [14], we consider an image as a function f on a rectangular grid \mathbb{Z}^2 and a feature map as a function on a group G . In group-theoretic terms, the first layer in a convolutional network can be written as,

$$[f * \psi](g) = \sum_{y \in \mathbb{Z}^2} \sum_{k=1}^K f_k(y) \psi_k(g^{-1}y), \quad (1)$$

where K is the number of filters, ψ_k is the k th filter, and $g^{-1}y$ is the inverse group action of element g on $y \in \mathbb{Z}^2$, i.e., $g^{-1}y = y - g$.

By considering g to be a member of $p4$ or $p4m$, a group-convolution maps input feature maps on \mathbb{Z}^2 to output feature maps $f * \psi$ on the respective group. When both ψ and f are functions on a group G , a group-convolution can be defined as,

$$[f * \psi](g) = \sum_{h \in G} \sum_{k=1}^K f_k(h) \psi_k(g^{-1}h). \quad (2)$$

Finally, for tasks such as segmentation and generation, it is necessary to bring the domain of feature maps from G back to \mathbb{Z}^2 . We can pool the feature map for each filter over the set of transformations, using either average or maximum values, corresponding to average or max pooling over the group. A transformation from G to \mathbb{Z}^2 can also be learned [36], but we did not notice an immediate benefit to doing so in our experiments and hence only use group pooling.

GAN optimization and stability. Several techniques have been proposed to stabilize the training of GANs. As we focus on the limited data setting where training instability is exacerbated across a diverse set of image resolutions, we briefly describe the two major stabilizing methods used in all experiments here.

We regularize the discriminator by using a zero-centered gradient penalty (GP) on the real data as proposed by [39] of the form,

$$R_1 := \frac{\gamma}{2} \mathbb{E}_{x \sim \mathbb{P}_{real}} [\|\nabla D(x)\|_2^2], \quad (3)$$

where γ is the regularization weight, x is sampled from the real distribution \mathbb{P}_{real} , and D is the discriminator. This GP has been shown to cause convergence (in toy cases), alleviate catastrophic forgetting [55], and strongly stabilize GAN training. However, empirical work has found that this GP achieves stability at the cost of worsening GAN evaluation scores [9]. Therefore, we use conservative γ values in all experiments to balance training stability and sample fidelity.

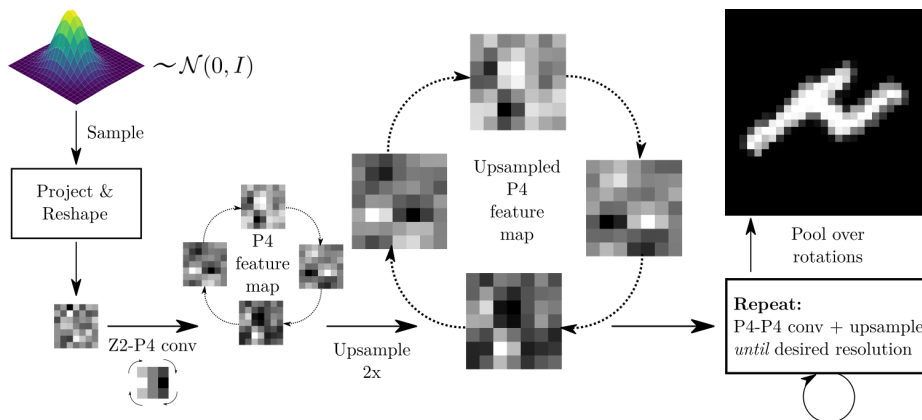


Fig. 2. An abbreviated illustration of group-convolutions used in our generator networks. Visual design inspired by [58].

A crucial and widely used technique for GAN stabilization is spectral normalization [41], which constrains the discriminator to be 1-Lipschitz, thereby improving the gradient feedback to the generator [66, 12]. With spectral normalization, each layer is rescaled as,

$$W_{SN} = W/\sigma(W), \quad (4)$$

where W is the weight matrix for a given layer and $\sigma(W)$ is its spectral norm. In practice, $\sigma(W)$ is estimated via a power iteration method as opposed to computing the full singular value decomposition during each training iteration. Finally, applying spectral normalization to both generator and discriminator empirically stabilizes and improves training significantly [65].

3.2 Group Equivariant Generative Adversarial Networks

In this section, we outline how to induce a symmetry prior into the generative adversarial framework and thus improve synthesis for globally-symmetric images. The literature has developed several techniques for regularization, normalization, and conditioning of the individual networks, along with their unique architectural choices - we extend these developments to the equivariant setting.

We start by replacing all convolutional layers with group-convolutional layers where filters and feature maps are functions on a pre-defined symmetry group G . Following [14], batch normalization moments [24] are calculated per group-feature map as opposed to each spatial feature map. Pointwise nonlinearities preserve equivariance for the groups considered here. Pre-activation residual blocks common to modern GANs are used freely as the sum of equivariant feature maps on G is also equivariant.

Generator. We use a fully connected layer to linearly project and reshape the concatenated noise vector $z \sim \mathcal{N}(0, I)$ and class embedding c into spatial feature maps on \mathbb{Z}^2 . We then use spectrally-normalized group-convolutions, interspersed with pointwise-nonlinearitys, and nearest-neighbours upsampling to increase spatial extent. We use upsampling followed by group-convolutions instead of transposed group-convolutions to reduce checkerboard artefacts [45]. We further use a novel group-equivariant class-conditional batch normalization layer (described below) to normalize and class-condition image generation while also projecting the latent vector z to each level of the group-convolutional hierarchy. We finally max-pool over the set of transformations to obtain the generated image $x \in \mathbb{Z}^2$. This process is illustrated at a high-level in Figure 2.

Discriminator. The group-equivariant discriminator receives an input $x \in \mathbb{Z}^2$, which it maps to a scalar indicating whether it is real or fake. We do this via spectrally normalized group-convolutions, pointwise-nonlinearitys, and spatial-pooling layers to decrease spatial extent. After the final group-convolutional layer, we pool over the group and use global average pooling to obtain an invariant representation at the output. Finally, we condition the discriminator output via the projection method proposed by [42].

Importantly, the equivariance of group-convolutions depends on the convolutional stride. Strided convolutions were commonly used for downsampling in early GANs [47]. However, stride values must be adjusted to the dataset to preserve equivariance, which makes comparisons to equivalent non-equivariant GAN architectures difficult. We therefore use pooling layers over the plane (commonly used in recent GANs) to downsample in all settings to preserve equivariance and enable a fair comparison.

Spectral Normalization. As the singular values of a matrix are invariant under compositions of 90-degree rotations, transpositions, and reflections - spectral normalization on a group-feature map preserves equivariance and we use it freely.

Class-conditional Batch Normalization. Conditional batch normalization [46] replaces the scale and shift of features with an affine transformation learned from the class label (and optionally from the latent vector as well [9]) via linear dense layers, and is widely used in generative networks. We propose a group-equivariance preserving conditional normalization by learning the affine transformation parameters per group-feature map, rather than each spatial feature. As we use fewer group-filters than equivalent non-equivariant GANs, we use fewer dense parameters to learn conditional scales and shifts.

4 Experiments

4.1 Preliminaries

Datasets. We focus on image datasets which possess roto(-reflective) symmetry, such that the image label is invariant under the corresponding transforma-

Table 1. A summary of the datasets considered in this paper. The right-most column indicates whether the dataset has a preferred pose.

Dataset	Resolution	n_{classes}	n_{training}	n_{testing}	Pose Preference
Rotated MNIST [33]	(28, 28)	10	12,000	50,000	No
ANHIR [1]	(128, 128, 3)	5	28,407	9,469	No
LYSTO [13]	(256, 256, 3)	3	20,000	-	No
Food-101 [8]	(64, 64, 3)	101	75,747	25,250	Yes

tion. This excludes datasets like ImageNet [16], CIFAR-10 [31], CelebA [37], and LSUN [64], as their images have a preferred orientation. For example, images in the `boat` class of CIFAR-10 cannot be upside-down. We evaluate conditional synthesis on small datasets which possess roto(-reflective) symmetry, or repurpose images from publicly available databases as detailed in Table 1.

Evaluation methodologies. GANs are commonly evaluated by embedding the real and generated images into the feature space of an ImageNet pre-trained network and computing similarity scores. The Fréchet Inception Distance (FID) [21] jointly captures sample fidelity and diversity and is presented for all experiments. To explicitly evaluate both aspects, we further present the improved precision and recall scores [32] for the RGB experiments. As the image categories considered here are not well-represented in ImageNet, we finetune Inception-v3 [54] on the relevant dataset unless otherwise stated. Finally, we perform ablation studies on all datasets to evaluate group-equivariance in either or both networks.

Setups. In each subsection, we list design choices made for individual experiments with full details available in Appendix B. We use recent methodologies for GAN training inspired by [9] to produce a strong non-equivariant baseline. We then modify either generator (G) and/or discriminator (D) as in Section 3.2 to obtain the corresponding equivariant settings.

The number of group-filters in each layer is divided by the square root of the size of the symmetry set to keep the number of parameters similar across settings. We skew towards stabilizing training for all settings to compare models under the same settings, thus obviating extensive checkpointing and hyperparameter optimization. We do not employ data augmentation in any experiment, as one of our goals is to evaluate generation with limited data.

Optimization is performed via Adam [30] with $\beta_1 = 0.0$ and $\beta_2 = 0.9$, as in [65, 9]. All discriminators are updated twice per generator update. We follow [21] and employ unequal learning rates η_G and η_D for generator and discriminator, respectively. We use an exponential moving average ($\alpha = 0.9999$) of generator weights across iterations when sampling images, as in [9, 29, 63]. All initializations use the same random seed. Generator models are saved for evaluation at every training epoch.

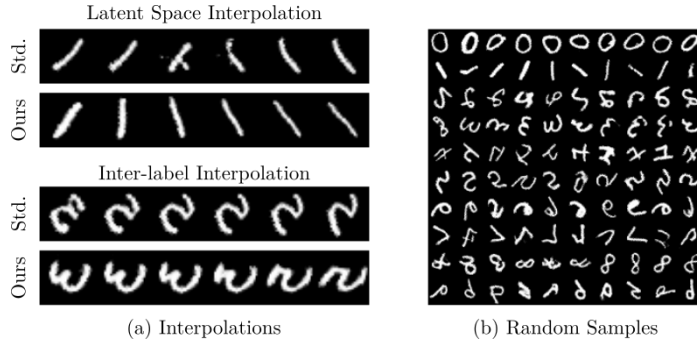


Fig. 3. Qualitative Rotated MNIST results. **(a)** Selected spherical interpolations [61] between generated samples in either latent space (**top**) or between labels (**bottom**). Group equivariant GANs interpolate intuitively between samples, whereas standard GANs do not. **(b)** Random samples from a group equivariant GAN trained with the full dataset and the relativistic average loss. Samples are drawn from a mildly truncated normal distribution ($\sigma = 0.75$) for visualization [9].

4.2 Rotated MNIST

Rotated MNIST [33] provides random rotations of the MNIST dataset and is a common benchmark for equivariant CNNs [14, 60]. We use a diversity of training scenarios to evaluate the sensitivity of equivariance to GAN experimental design. These results later motivate our choices for higher resolution synthesis.

Experimental Setup. We experiment with three different proportions of training data: 33%, 66%, and 100%. The non-saturating loss from [19] (NSGAN), the dual-formulation Wasserstein loss [2] (WGAN), and the relativistic average loss [28] (RaGAN) are tested. With the NSGAN and RaGAN loss, we use the R_1 GP, conservatively setting $\gamma = 0.1$. For the WGAN loss, we use the GP defined in [20] to ensure the Lipschitz constraint with the recommended weight of 10.0.

Implementation. Given the low resolution of Rotated MNIST, we take a straightforward approach. In the generator, we sample from a $64D$ Gaussian latent space, concatenate class embeddings, and linearly project as described in Section 3.2. Four spectrally-normalized convolutional layers are then used with class-conditional batch normalization employed after every convolution except for the first and last layer. The discriminator uses three spectrally normalized convolutional layers, with leaky ReLU non-linearities. Average pooling is used to reduce the spatial extent of the feature maps, with global average pooling and conditional projection used at the end of the sequence.

For the group-equivariant setting, all convolutions are replaced with $p4$ -convolutions. $p4m$ is precluded as some digits do not possess reflective symmetry. Max-pooling over rotations is used after the last group-convolutional layer in both generator and discriminator to get \mathbb{Z}^2 feature maps. All settings were

Table 2. Minimum and mean values of the Fréchet distance (lower is better) of generated Rotated MNIST samples, evaluated at every 1K generator iterations until 20K. In every configuration tested, using $p4$ -equivariant convolutional layers improves FID. A boxplot containing all results is given in Appendix A.

Loss	Generator Discriminator		Min. & Mean Fréchet Distance		
			Available Training Data		
			33%	66%	100%
NSGAN-GP	CNN	CNN	(0.68, 8.15)	(0.84, 7.70)	(0.94, 8.36)
		CNN	(1.07, 3.59)	(0.55, 2.89)	(0.49, 3.23)
		G-CNN	(0.89, 7.47)	(0.82, 7.47)	(0.81, 7.64)
		G-CNN	(0.61, 4.94)	(0.99, 3.40)	(0.73, 3.65)
RAGAN-GP	CNN	CNN	(1.34, 11.95)	(0.95, 10.98)	(1.28, 11.68)
		CNN	(0.84, 3.23)	(0.36, 2.84)	(0.56, 3.06)
		G-CNN	(1.26, 9.14)	(0.86, 8.81)	(0.98, 9.95)
		G-CNN	(0.73, 3.46)	(0.61, 2.81)	(0.57, 2.94)
WGAN-GP	CNN	CNN	(3.43, 18.13)	(4.28, 17.77)	(4.99, 19.43)
		CNN	(0.76, 4.32)	(0.57, 3.63)	(0.29, 3.65)
		G-CNN	(3.16, 17.47)	(3.12, 17.82)	(2.88, 17.50)
		G-CNN	(0.58, 3.37)	(0.52, 3.66)	(0.58, 3.59)

trained for 20,000 generator iterations with a batch size of 64. Learning rates were set to $\eta_G = 0.0001$ and $\eta_D = 0.0004$, respectively.

Results. We use features derived from the final pooling layer of the $p4$ -CNN defined in [14] to replace Inception-featurization. An analogous approach was taken in [6] in their MNIST experiments. Fréchet distance of synthesized samples to the test set is calculated at every thousand generator iterations.

As shown in Table 2, we find that under every configuration of loss and data availability considered, using $p4$ -convolutions in either network improves both the mean and minimum Fréchet distance. Most of the gains to be made come from using a $p4$ -equivariant discriminator, with the addition of a $p4$ -equivariant generator only helping in a few cases. However, this may be due to the dataset being a relatively simple benchmark. The NSGAN-GP and RAGAN-GP losses perform similarly, with WGAN-GP underperforming initially and ultimately achieving comparable results. This may be due to using fewer discriminator updates per generator iteration than in the original WGAN-GP.

Qualitatively, the equivariant model learns better representations as shown in Figure 3(a). Holding the class-label constant and interpolating between samples, we find that the non-equivariant GAN changes the shape of the digit in order to rotate it, whereas the equivariant model learns rotation in the latent space. Similarly, holding the latent vector constant and interpolating between classes shows that our model learns an intuitive interpolation between digits, whereas the non-equivariant model transforms the image immediately.

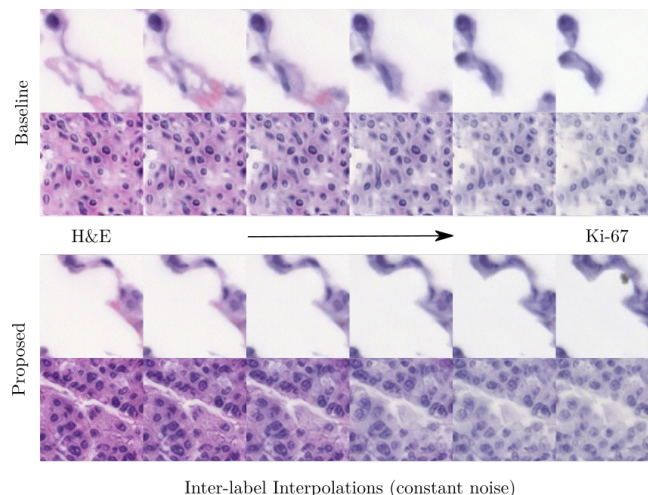


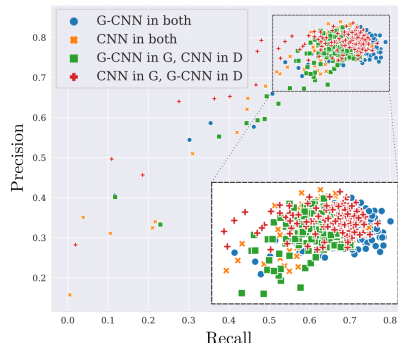
Fig. 4. Selected inter-label linear interpolations [61] between two staining dyes in synthesized ANHIR images, while holding the sampled noise vector constant. The non-equivariant model (**top**) changes both structure and dye between the generated samples, whereas the group-equivariant model (**bottom**) better preserves structure while translating between dyes. This corresponds to the equivariant model learning representations that better disentangle structure and appearance (staining dye).

4.3 ANHIR

ANHIR is an image registration challenge which provides high-resolution digital pathology slides stained with five different dyes to highlight different cellular properties [1, 7]. We extract 128×128 foreground patches from two whole slide images imaged at different scales, with methodology described in Appendix B. We use the staining dye as a source of class conditioning.

Implementation. We sample from a $128D$ Gaussian latent space with a batch size of 32. The generator consists of 6 pre-activation residual blocks detailed in Appendix B, followed by a final convolutional layer to obtain a 3-channel output. We use class-conditional batch normalization after every convolution, except at the final layer. The discriminator uses 5 pre-activation residual blocks, followed by global average pooling and conditional projection. In the equivariant settings, we use residual blocks with $p4m$ -convolutions for roto-reflective symmetries. We train with the relativistic average loss and use the R_1 GP with $\gamma = 0.1$. Learning rates are set to $\eta_G = 0.0001$ and $\eta_D = 0.0004$.

Results. Quantitative results are presented in Figure 5. We find that $p4m$ -equivariance in either network improves FID evaluation, with the best results coming from modifying both networks. From the white inset in Figure 5, we see that $p4m$ -equivariance in both networks consistently achieves higher recall. As



Setting	FID _{min}
CNN in G and D	7.32
G-CNN in G , CNN in D	6.93
CNN in G , G-CNN in D	5.56
G-CNN in G and D	5.54

Fig. 5. Quantitative ANHIR evaluation. **Left:** Precision and recall plots for all snapshots of trained models in each setting (closer to top-right is better). **Right:** FID results for each setting (lower is better).

the differences between classes in this dataset should be primarily stain (color) based, we visualize inter-class interpolations between synthesized samples in Figure 4. We find that our model better preserves structure while translating between stains, whereas the non-equivariant GAN struggles to do so. Random samples are provided in Appendix A.

4.4 LYSTO

LYSTO is a digital pathology challenge dataset for benchmarking the counting of immunohistochemistry stained lymphocytes across multiple organs [13]. We re-purpose it here for conditional image synthesis at a higher resolution of 256×256 . As classification labels are not provided, we use the organ source as class labels. The use of organ sources as classes is validated in Appendix B. The high image resolution in addition to the limited sample size of 20,000 make LYSTO a challenging dataset for GANs.

Implementation. The implementation of this experiment is similar to that of Section 4.3, with some key differences due to the greater difficulty of training. Due to memory constraints, we use a batch size of 16. We increase the number of residual blocks to 6 in both generator and discriminator and halve the number of filters. The equivariant settings used the $p4m$ roto-reflective symmetries.

We initially experienced low sample diversity across a variety of hyperparameter settings. Contrary to recent literature, we find that using batch normalization in the discriminator in addition to spectral normalization greatly improves training for this dataset. Further, halving the learning rates for both networks to $\eta_G = 0.00005$ and $\eta_D = 0.0002$ and increasing the strength of the gradient penalty to 1.0 were necessary for training stability.

Results. As the labels for the testing set are not publicly available, we evaluate generated samples with respect to the training set itself in Figure 7 as in [28]. We

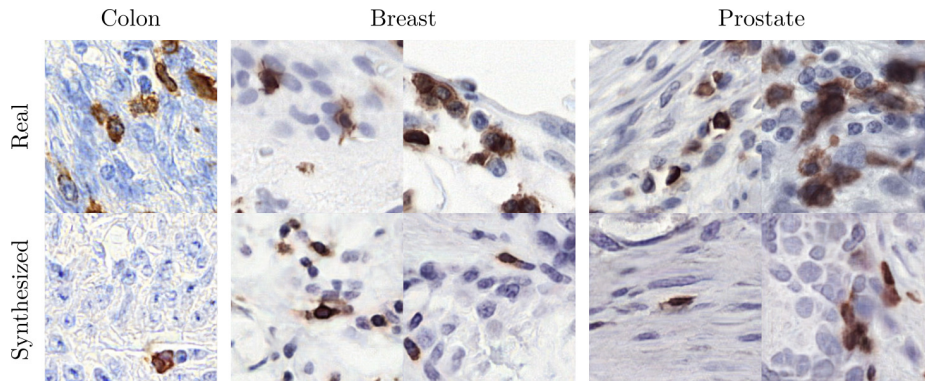
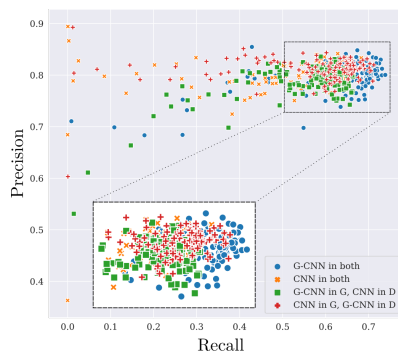


Fig. 6. Qualitative selected samples for 256×256 conditional image synthesis with the LYSTO dataset. Random samples are available in Appendix A.



Setting	FID _{min}
CNN in G and D	7.27
G-CNN in G , CNN in D	6.68
CNN in G , G-CNN in D	5.02
G-CNN in G and D	3.90

Fig. 7. Quantitative LYSTO evaluation. **Left:** Precision and recall plots for all snapshots of trained models in each setting (closer to top-right is better). **Right:** FID results for each setting (lower is better).

find that the model using $p4m$ -convolutions in both G and D has the best performance in terms of FID and achieves consistently higher recall. In all settings, we find that $p4m$ -convolutions improve FID. As in Section 4.3, the effects on precision and recall are more subtle and we find that $p4m$ -convolutions in both networks consistently achieves higher recall with similar precision. Qualitative synthesized samples are visualized in Figure 6.

4.5 Food-101

Food-101 [8] is a small natural image dataset of a 101 categories of food taken in various challenging settings of over/under exposure, label noise, etc. Further, datasets with a high number of classes are known to be challenging for GANs [44]. Importantly, even though the objects in this dataset have a preferred pose due to common camera orientations, we speculate that roto-equivariance may be

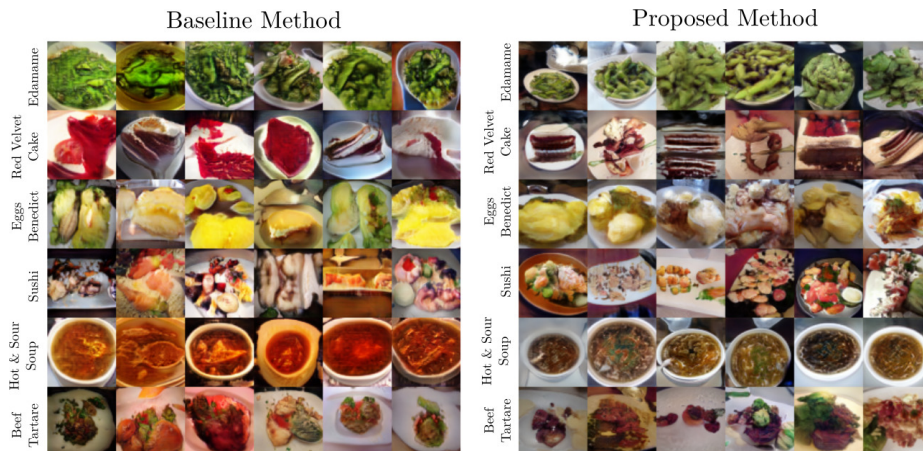


Fig. 8. Random samples from arbitrary categories drawn from the best performing non-equivariant GAN (**left**) and $p4$ -equivariant GAN (**right**). Samples are drawn from a truncated normal distribution ($\sigma = 0.75$) for visualization purposes. Readers are encouraged to zoom in to highlight differences in sample diversity and fidelity.

beneficial here as food photography commonly takes an *en face* or mildly oblique view. We resize the training set to 64×64 resolution for our experiments.

Implementation. Compared to the residual synthesis models in Sections 4.3 and 4.4, we make several changes. We sample from a $64D$ latent Gaussian to lower the number of dense parameters and substantially increase the width of the residual blocks to account for the high number of image classes. We find that an $8\times$ increase in the number of channels for the initial projection from the latent vector and class embedding improves training significantly. We use 4 residual blocks each in both generator and discriminator. For the equivariant setting, we use only $p4$ rotational symmetries to reduce training time. Importantly, we increase the batch size to 64 and the R_1 GP to $\gamma = 1.0$, both of which improve the evaluation of all experimental settings.

Results. As several classes of food are represented in ImageNet, we use the official `TensorFlow` weights for feature extraction for FID, precision, and recall. Interestingly, we find that the two settings using $p4$ -equivariance in D generate images at an arbitrary but largely consistent pose for all classes, subject to random initialization. E.g., in the `G-CNN` in both setting in Figure 9, all images synthesized were rotated 180-degrees relative to human perception. This rotational-ambiguity may be anticipated as a rotation equivariant D assigns the same probability of being real to a natural image and its rotated counterparts. As the rotation of the generated samples is consistent for all samples, we speculate that this corresponds to a local optimum of G , leaving an in-depth exploration of this phenomenon to future work.

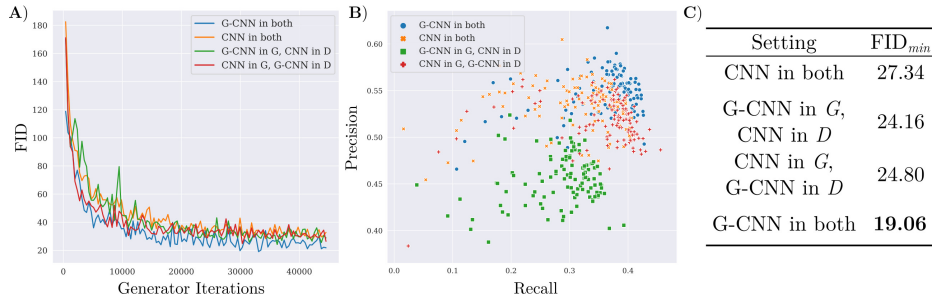


Fig. 9. Quantitative results for image synthesis with Food-101. **A)** FID evaluations across generator iterations. **B)** Precision vs. recall scatterplot of all model snapshots (closer to top-right is better). **C)** Best FID results for each setting (lower is better).

As Inception-v3 features are not rotation invariant, the samples generated by models with $p4$ -equivariant D s perform slightly worse than their non-equivariant counterparts. However, when simply rotated back to their natural pose, we improve on the baseline non-equivariant setting significantly, consistently improving on the baseline model across generator iterations and achieving an 8+ point improvement in FID as shown in Figure 9. A comparison of the original and pose-adjusted settings can be found in Appendix A. Finally, we find a larger improvement between the **G-CNN in both** setting and others in terms of precision and recall than in Sections 4.3 and 4.4.

5 Discussion

In this paper, we present a flexible framework for incorporating roto(-reflective) symmetry within GANs. In doing so, we empirically improve the sample complexity of GANs when trained on globally-symmetric images. Our experiments confirm this by improving on conventional GANs in sample fidelity and diversity across a variety of datasets, ranging from medical imaging modalities to real-world images of food. Modifying either generator or discriminator lead to improvements in FID, with the latter having more impact. We find that making both networks group-equivariant consistently yields the best results across various scores and more intuitive interpolations in latent space.

To our knowledge, our work is the first to scale equivariant learning to high-resolution generation. We focus on conditional image synthesis, but our methods can easily be extended to other GAN tasks such as image-to-image translation and super-resolution. In future work, we will incorporate long-range dependencies within our model as attention has been successfully used within GANs [65]. Fortunately, several formulations of self-attention are translation-equivariant and contemporaneous work has proposed group-attention mechanisms [49, 48] which may be applicable to generative modeling. Finally, we will extend our approach to include equivariance to continuous groups [60], which may yield further increased data efficiency and more powerful representations.

References

1. ANHIR Grand Challenge. <https://anhir.grand-challenge.org/>, [Online; accessed: 2020-03-01]
2. Arjovsky, M., Chintala, S., Bottou, L.: Wasserstein gan. arXiv preprint arXiv:1701.07875 (2017)
3. Bass, C., Dai, T., Billot, B., Arulkumaran, K., Creswell, A., Clopath, C., De Paola, V., Bharath, A.A.: Image synthesis with a convolutional capsule generative adversarial network
4. Beaufort, Jean: Spiral galaxy, <https://www.publicdomainpictures.net/en/view-image.php?image=181054&picture=spiral-galaxy>, [Online; accessed Feb 10, 2020.]
5. Bietti, A., Mairal, J.: Group invariance, stability to deformations, and complexity of deep convolutional representations. *The Journal of Machine Learning Research* **20**(1), 876–924 (2019)
6. Binkowski, M., Sutherland, D.J., Arbel, M., Gretton, A.: Demystifying MMD GANs. In: 6th International Conference on Learning Representations, ICLR 2018, Vancouver, BC, Canada, April 30 - May 3, 2018, Conference Track Proceedings (2018)
7. Borovec, J., Munoz-Barrutia, A., Kybic, J.: Benchmarking of image registration methods for differently stained histological slides. In: 2018 25th IEEE International Conference on Image Processing (ICIP). pp. 3368–3372. IEEE (2018)
8. Bossard, L., Guillaumin, M., Van Gool, L.: Food-101 – mining discriminative components with random forests. In: European Conference on Computer Vision (2014)
9. Brock, A., Donahue, J., Simonyan, K.: Large scale gan training for high fidelity natural image synthesis. arXiv preprint arXiv:1809.11096 (2018)
10. Chen, T., Zhai, X., Ritter, M., Lucic, M., Houlsby, N.: Self-supervised gans via auxiliary rotation loss. In: Proceedings of the IEEE Conference on Computer Vision and Pattern Recognition. pp. 12154–12163 (2019)
11. Chidester, B., Ton, T.V., Tran, M.T., Ma, J., Do, M.N.: Enhanced rotation-equivariant u-net for nuclear segmentation. In: Proceedings of the IEEE Conference on Computer Vision and Pattern Recognition Workshops. pp. 0–0 (2019)
12. Chu, C., Minami, K., Fukumizu, K.: Smoothness and stability in gans. In: International Conference on Learning Representations (2020), <https://openreview.net/forum?id=HJeOekHKwr>
13. Ciompi, F., Jiao, Y., van der Laak, J.: Lymphocyte assessment hackathon (lysto) (Oct 2019). <https://doi.org/10.5281/zenodo.3513571>, <https://doi.org/10.5281/zenodo.3513571>
14. Cohen, T., Welling, M.: Group equivariant convolutional networks. In: International conference on machine learning. pp. 2990–2999 (2016)
15. Cohen, T.S., Geiger, M., Weiler, M.: A general theory of equivariant cnns on homogeneous spaces. In: Advances in Neural Information Processing Systems. pp. 9142–9153 (2019)
16. Deng, J., Dong, W., Socher, R., Li, L.J., Li, K., Fei-Fei, L.: ImageNet: A Large-Scale Hierarchical Image Database. In: CVPR09 (2009)
17. Dieleman, S., De Fauw, J., Kavukcuoglu, K.: Exploiting cyclic symmetry in convolutional neural networks. arXiv preprint arXiv:1602.02660 (2016)
18. Dieng, A.B., Ruiz, F.J., Blei, D.M., Titsias, M.K.: Prescribed generative adversarial networks. arXiv preprint arXiv:1910.04302 (2019)
19. Goodfellow, I., Pouget-Abadie, J., Mirza, M., Xu, B., Warde-Farley, D., Ozair, S., Courville, A., Bengio, Y.: Generative adversarial nets. In: Advances in neural information processing systems. pp. 2672–2680 (2014)

20. Gulrajani, I., Ahmed, F., Arjovsky, M., Dumoulin, V., Courville, A.C.: Improved training of wasserstein gans. In: *Advances in neural information processing systems*. pp. 5767–5777 (2017)
21. Heusel, M., Ramsauer, H., Unterthiner, T., Nessler, B., Hochreiter, S.: Gans trained by a two time-scale update rule converge to a local nash equilibrium. In: *Advances in Neural Information Processing Systems*. pp. 6626–6637 (2017)
22. Hillewaert, Hans: *Asterias rubens* Linnaeus, 1758, =<http://www.marinespecies.org/aphia.php?p=image&pic=653>, [Online; accessed Feb 10, 2020.]
23. Hinton, G.E., Krizhevsky, A., Wang, S.D.: Transforming auto-encoders. In: *International Conference on Artificial Neural Networks*. pp. 44–51. Springer (2011)
24. Ioffe, S., Szegedy, C.: Batch normalization: Accelerating deep network training by reducing internal covariate shift. *arXiv preprint arXiv:1502.03167* (2015)
25. Isola, P., Zhu, J.Y., Zhou, T., Efros, A.A.: Image-to-image translation with conditional adversarial networks. In: *Proceedings of the IEEE conference on computer vision and pattern recognition*. pp. 1125–1134 (2017)
26. Jaderberg, M., Simonyan, K., Zisserman, A., et al.: Spatial transformer networks. In: *Advances in neural information processing systems*. pp. 2017–2025 (2015)
27. Jaiswal, A., AbdAlmageed, W., Wu, Y., Natarajan, P.: CapsuleGAN: Generative adversarial capsule network. In: Leal-Taixé, L., Roth, S. (eds.) *Computer Vision – ECCV 2018 Workshops*. Springer International Publishing, Cham (2019)
28. Jolicoeur-Martineau, A.: The relativistic discriminator: a key element missing from standard gan. *arXiv preprint arXiv:1807.00734* (2018)
29. Karras, T., Aila, T., Laine, S., Lehtinen, J.: Progressive growing of gans for improved quality, stability, and variation. *arXiv preprint arXiv:1710.10196* (2017)
30. Kingma, D.P., Ba, J.: Adam: A method for stochastic optimization. *arXiv preprint arXiv:1412.6980* (2014)
31. Krizhevsky, A., et al.: Learning multiple layers of features from tiny images (2009)
32. Kynkäänniemi, T., Karras, T., Laine, S., Lehtinen, J., Aila, T.: Improved precision and recall metric for assessing generative models. In: *Advances in Neural Information Processing Systems*. pp. 3929–3938 (2019)
33. Larochelle, H., Erhan, D., Courville, A., Bergstra, J., Bengio, Y.: An empirical evaluation of deep architectures on problems with many factors of variation. In: *Proceedings of the 24th international conference on Machine learning*. pp. 473–480. ACM (2007)
34. Lenc, K., Vedaldi, A.: Understanding image representations by measuring their equivariance and equivalence. In: *Proceedings of the IEEE conference on computer vision and pattern recognition*. pp. 991–999 (2015)
35. Lin, C.H., Yumer, E., Wang, O., Shechtman, E., Lucey, S.: St-gan: Spatial transformer generative adversarial networks for image compositing. In: *Proceedings of the IEEE Conference on Computer Vision and Pattern Recognition*. pp. 9455–9464 (2018)
36. Linmans, J., Winkens, J., Veeling, B.S., Cohen, T.S., Welling, M.: Sample efficient semantic segmentation using rotation equivariant convolutional networks. *arXiv preprint arXiv:1807.00583* (2018)
37. Liu, Z., Luo, P., Wang, X., Tang, X.: Large-scale celebfaces attributes (celeba) dataset
38. Liu, Z., Luo, P., Wang, X., Tang, X.: Deep learning face attributes in the wild. In: *Proceedings of the IEEE international conference on computer vision*. pp. 3730–3738 (2015)

39. Mescheder, L., Geiger, A., Nowozin, S.: Which training methods for gans do actually converge? arXiv preprint arXiv:1801.04406 (2018)
40. Mirza, M., Osindero, S.: Conditional generative adversarial nets. arXiv preprint arXiv:1411.1784 (2014)
41. Miyato, T., Kataoka, T., Koyama, M., Yoshida, Y.: Spectral normalization for generative adversarial networks. arXiv preprint arXiv:1802.05957 (2018)
42. Miyato, T., Koyama, M.: cgans with projection discriminator. arXiv preprint arXiv:1802.05637 (2018)
43. Noguchi, A., Harada, T.: Image generation from small datasets via batch statistics adaptation. arXiv preprint arXiv:1904.01774 (2019)
44. Odena, A.: Open questions about generative adversarial networks. Distill (2019). <https://doi.org/10.23915/distill.00018>, <https://distill.pub/2019/gan-open-problems>
45. Odena, A., Dumoulin, V., Olah, C.: Deconvolution and checkerboard artifacts. Distill **1**(10), e3 (2016)
46. Perez, E., Strub, F., De Vries, H., Dumoulin, V., Courville, A.: Film: Visual reasoning with a general conditioning layer. In: Thirty-Second AAAI Conference on Artificial Intelligence (2018)
47. Radford, A., Metz, L., Chintala, S.: Unsupervised representation learning with deep convolutional generative adversarial networks. arXiv preprint arXiv:1511.06434 (2015)
48. Romero, D.W., Bekkers, E.J., Tomczak, J.M., Hoogendoorn, M.: Attentive group equivariant convolutional networks (2020)
49. Romero, D.W., Hoogendoorn, M.: Co-attentive equivariant neural networks: Focusing equivariance on transformations co-occurring in data. arXiv preprint arXiv:1911.07849 (2019)
50. Ronneberger, O., Fischer, P., Brox, T.: U-net: Convolutional networks for biomedical image segmentation. In: International Conference on Medical image computing and computer-assisted intervention. pp. 234–241. Springer (2015)
51. Russakovsky, O., Deng, J., Su, H., Krause, J., Satheesh, S., Ma, S., Huang, Z., Karpathy, A., Khosla, A., Bernstein, M., et al.: Imagenet large scale visual recognition challenge. International journal of computer vision **115**(3), 211–252 (2015)
52. Sabour, S., Frosst, N., Hinton, G.E.: Dynamic routing between capsules. In: Advances in neural information processing systems. pp. 3856–3866 (2017)
53. Simonyan, K., Zisserman, A.: Very deep convolutional networks for large-scale image recognition. arXiv preprint arXiv:1409.1556 (2014)
54. Szegedy, C., Vanhoucke, V., Ioffe, S., Shlens, J., Wojna, Z.: Rethinking the inception architecture for computer vision. In: Proceedings of the IEEE conference on computer vision and pattern recognition. pp. 2818–2826 (2016)
55. Thanh-Tung, H., Tran, T.: On catastrophic forgetting in generative adversarial networks. arXiv preprint arXiv:1807.04015 (2018)
56. Tran, L., Kossaifi, J., Panagakis, Y., Pantic, M.: Disentangling geometry and appearance with regularised geometry-aware generative adversarial networks. International Journal of Computer Vision (IJCV) **127**(6-7), 824–844 (2019)
57. Upadhyay, Y., Schrater, P.: Generative adversarial network architectures for image synthesis using capsule networks. arXiv preprint arXiv:1806.03796 (2018)
58. Veeling, B.S., Linmans, J., Winkens, J., Cohen, T., Welling, M.: Rotation equivariant cnns for digital pathology. In: International Conference on Medical image computing and computer-assisted intervention. pp. 210–218. Springer (2018)

59. Wang, Y., Wu, C., Herranz, L., van de Weijer, J., Gonzalez-Garcia, A., Raducanu, B.: Transferring gans: generating images from limited data. In: Proceedings of the European Conference on Computer Vision (ECCV). pp. 218–234 (2018)
60. Weiler, M., Cesa, G.: General e (2)-equivariant steerable cnns. In: Advances in Neural Information Processing Systems. pp. 14334–14345 (2019)
61. White, T.: Sampling generative networks. arXiv preprint arXiv:1609.04468 (2016)
62. Winkels, M., Cohen, T.S.: Pulmonary nodule detection in ct scans with equivariant cnns. *Medical image analysis* **55**, 15–26 (2019)
63. Wu, Y., Donahue, J., Balduzzi, D., Simonyan, K., Lillicrap, T.: Logan: Latent optimisation for generative adversarial networks. arXiv preprint arXiv:1912.00953 (2019)
64. Yu, F., Seff, A., Zhang, Y., Song, S., Funkhouser, T., Xiao, J.: Lsun: Construction of a large-scale image dataset using deep learning with humans in the loop. arXiv preprint arXiv:1506.03365 (2015)
65. Zhang, H., Goodfellow, I., Metaxas, D., Odena, A.: Self-attention generative adversarial networks. arXiv preprint arXiv:1805.08318 (2018)
66. Zhou, Z., Liang, J., Song, Y., Yu, L., Wang, H., Zhang, W., Yu, Y., Zhang, Z.: Lipschitz generative adversarial nets. In: Proceedings of the 36th International Conference on Machine Learning. pp. 7584–7593 (2019)

A Supplementary Results

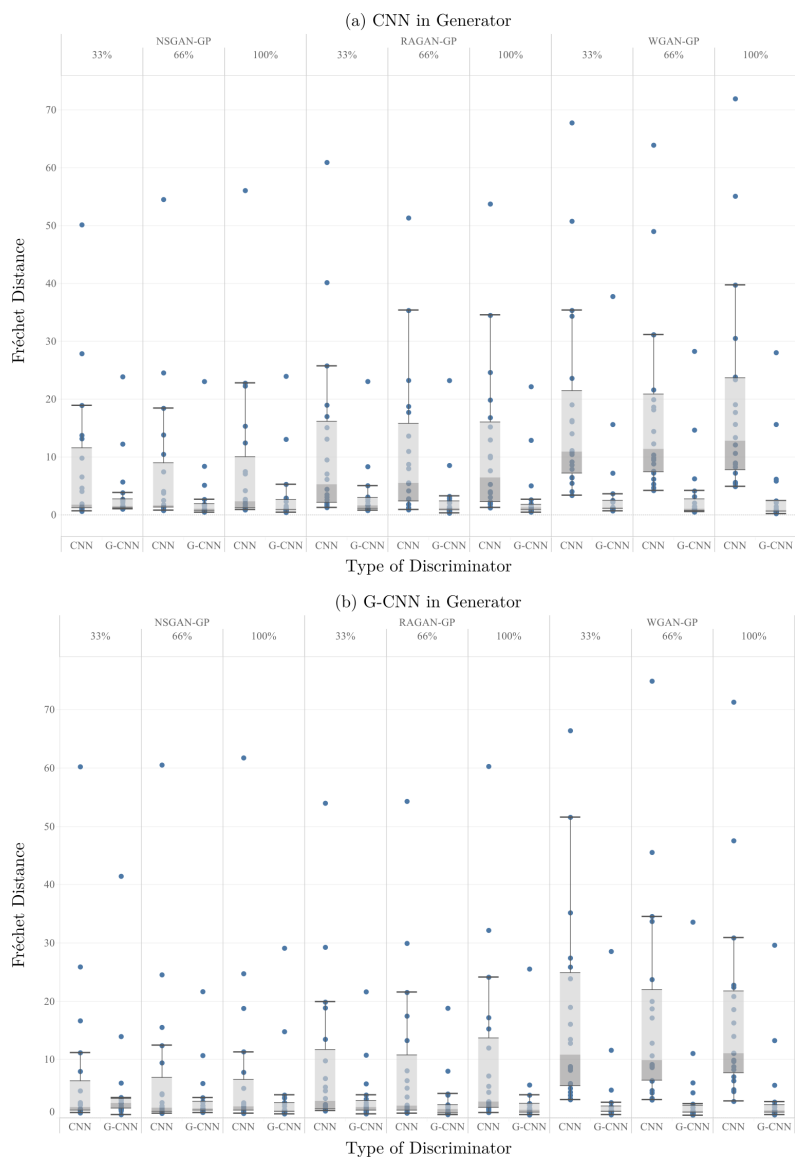


Fig. 10. A comparison of all GAN settings on Rotated MNIST. Each dot represents the Fréchet distance to the test set, which is evaluated every 1,000 generator iterations, for 20,000 iterations total. The top and bottom boxplots use a standard and group-equivariant CNN in the generator, respectively. In all settings, using a G-CNN in the discriminator lowers both mean and inter-quartile ranges for the Fréchet distance.

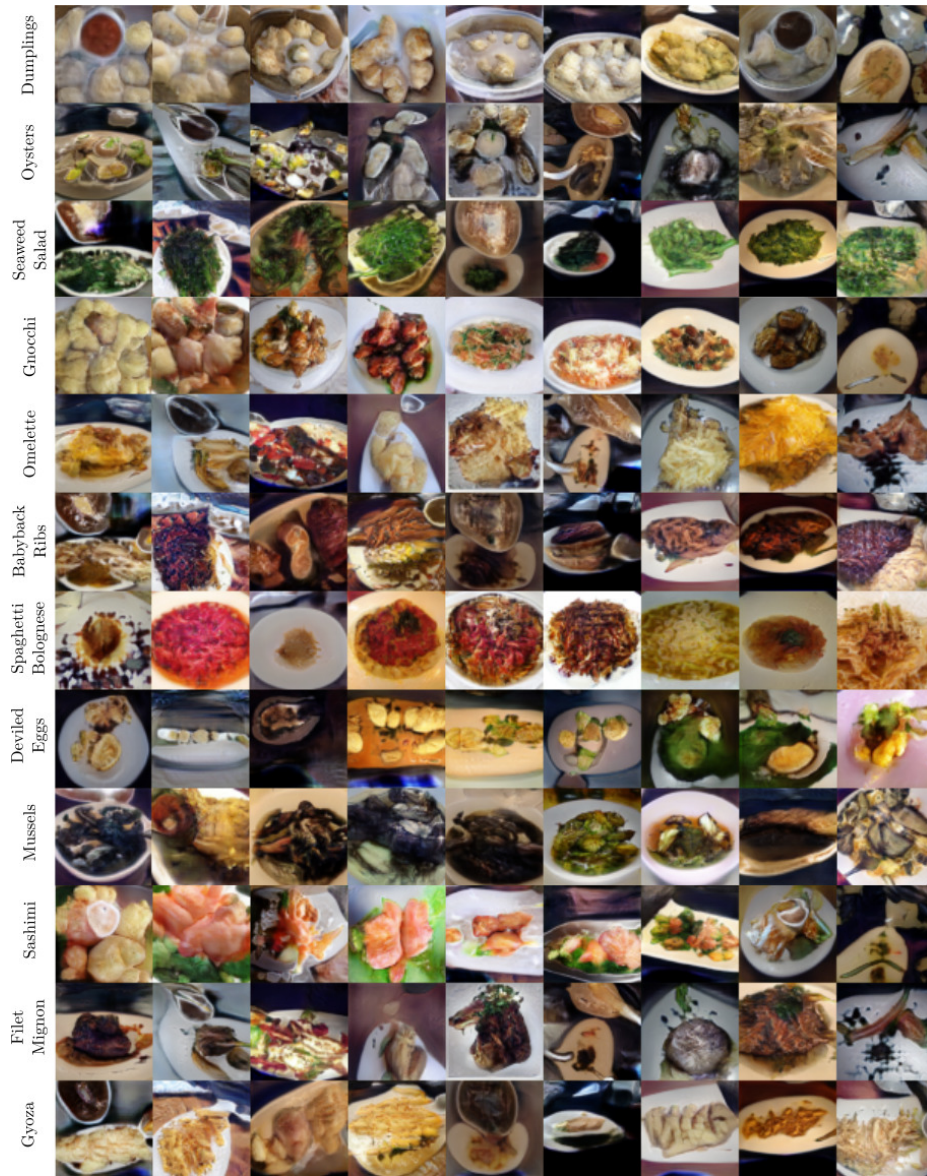


Fig. 11. Random 64×64 Food-101 samples with no truncation taken from the best performing model snapshot with $p4$ -equivariance in both generator and discriminator.

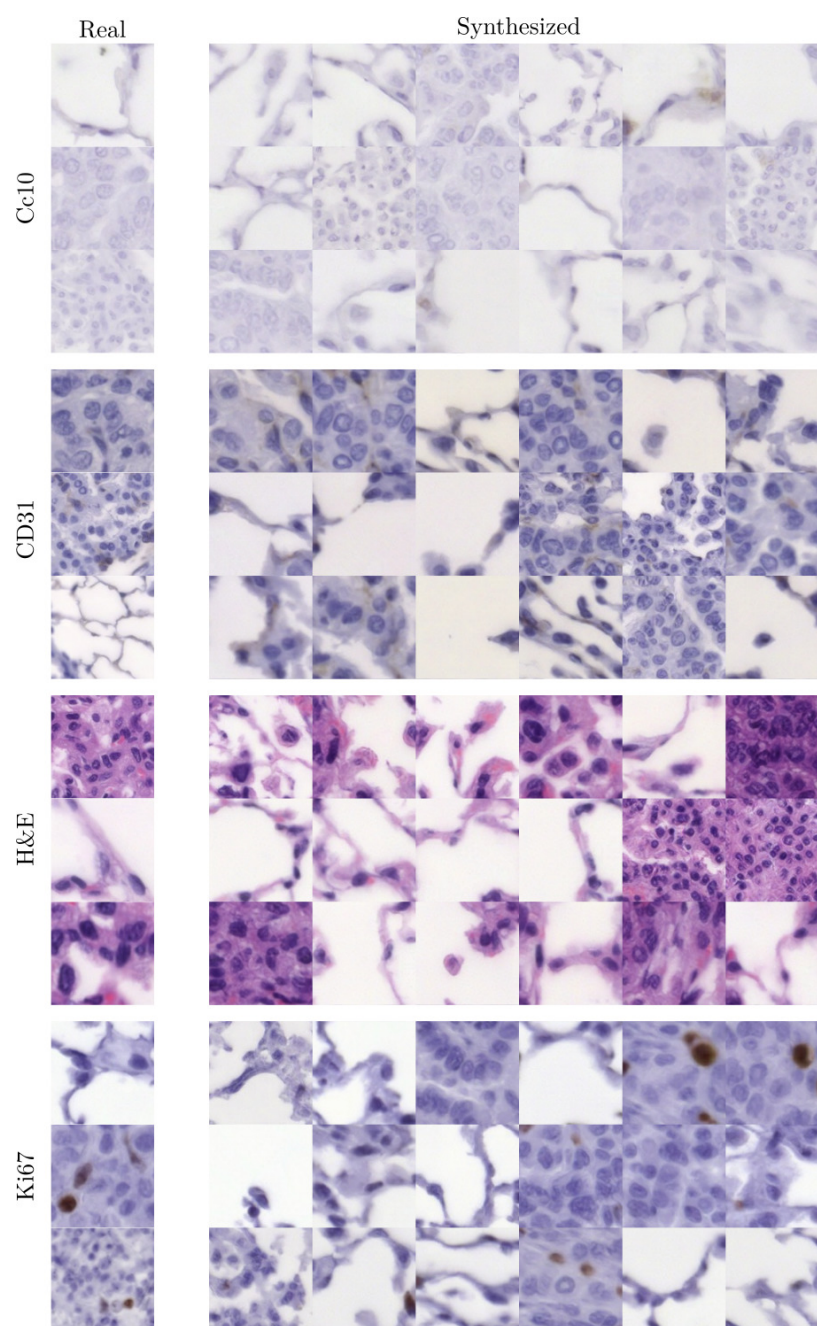


Fig. 12. Random 128×128 ANHIR samples with no truncation taken from the best performing model snapshot with $p4m$ -equivariance in both generator and discriminator. Selected real samples are shown in the left column for reference.

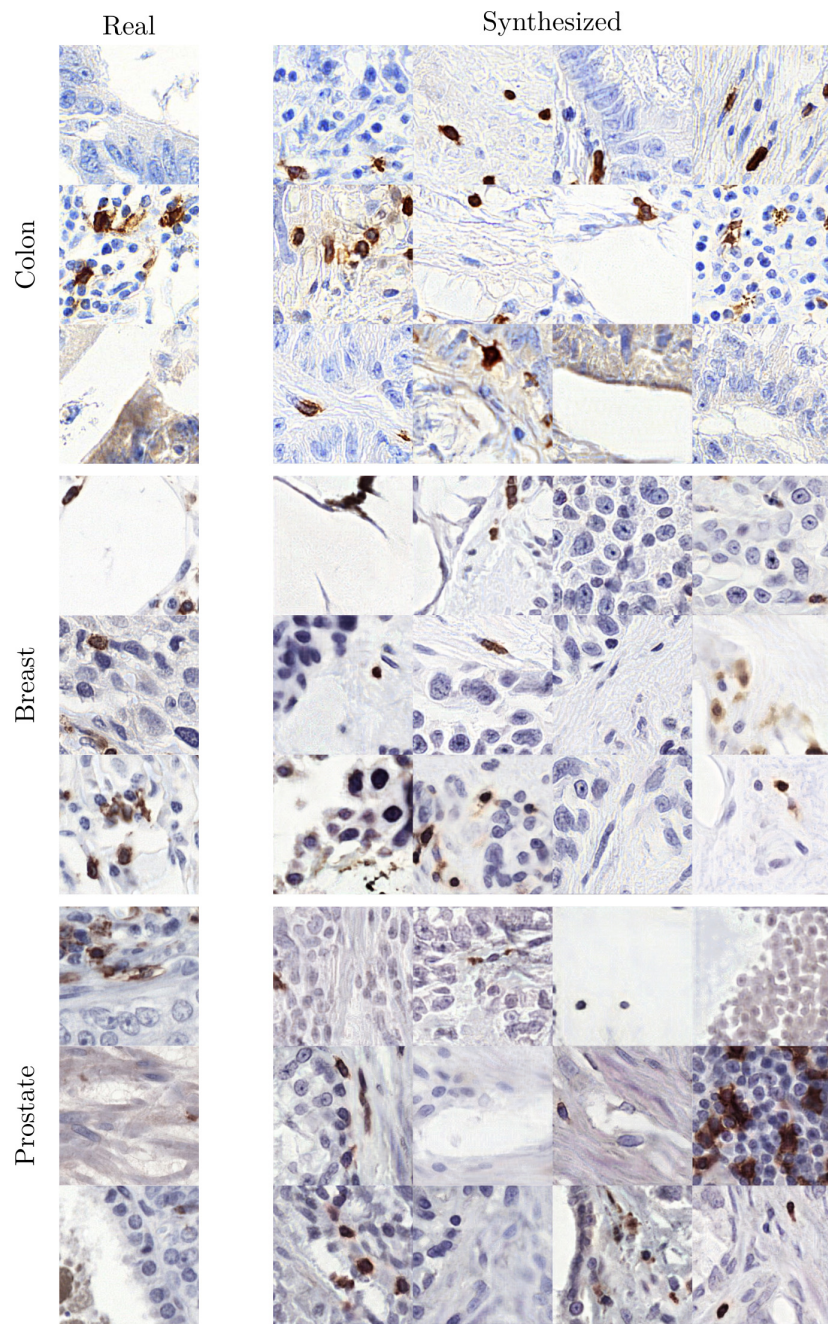


Fig. 13. Random 256×256 LYSTO samples with no truncation taken from the best performing model snapshot with $p4m$ -equivariance in both generator and discriminator. Selected real samples are shown in the left column for reference.

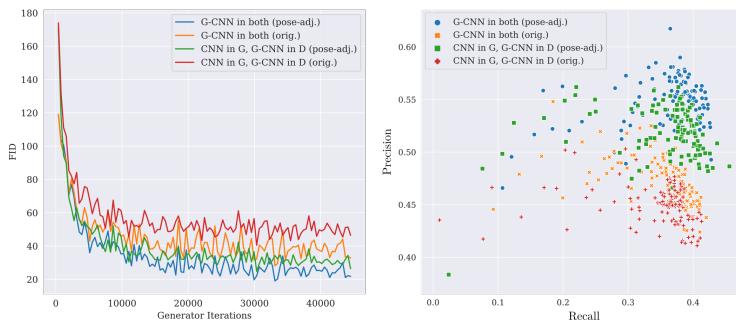


Fig. 14. A comparison of quantitative metrics on Food-101 synthesis before and after pose-adjustment for the settings which use a $p4$ -equivariant discriminator. When simply reoriented to their canonical pose, the scores are improved. We speculate that these scores are impacted as the Inception-v3 feature extractor is not rotation-invariant.

B Experimental details

B.1 Data preparation

B.1.1 LYSTO class conditioning To validate the assumption of the organ source being a discriminative feature, a suitable test would be to train a classifier to distinguish between sources. We partition the original training set with a 60/40 train/test split. The original testing set is not used as it has no publicly available organ source information. The dataset has 3 classes - colon, breast, and prostate. Holding out 20% of the new constructed training set for validation, we fine-tune VGG16 [53] (pre-trained on ImageNet) and achieve 98% organ source classification test accuracy, thus validating our assumption.

B.1.2 ANHIR patch extraction To extract patches for image synthesis, we choose the `lung-lesion` images from the larger ANHIR dataset, as these images are provided at different scales and possess diverse staining. The images were cropped to the nearest multiples of 128, and 128×128 patches were then extracted. Foreground/background masking was performed via K-means clustering, followed by morphological dilation. The images were then gridded into 128×128 patches, i.e., there was no overlap between patches. If a patch contained less than 10% foreground pixels, it was excluded from consideration.

B.2 Architectures

Architectures for the Rotated MNIST experiments are given in Tables 3 and 4, ANHIR in Tables 5 and 6, and LYSTO in Tables 7 and 8. The residual blocks used in ANHIR, LYSTO, and Food-101 experiments are given in Figure 15. SN refers to spectral normalization and $(z2-p4)$, $(p4-p4)$, $(z2-p4m)$, $(p4m-p4m)$ refer to the type of convolution used. Batch normalization momentum is set to 0.1, and LeakyReLU slopes are set to 0.2 (if used).

Generator	Discriminator
Sample $z \in \mathbb{R}^{64} \sim \mathcal{N}(0, I)$	Input RGB image $x \in \mathbb{R}^{28 \times 28 \times 1}$
Embed $y \in \{0, \dots, 9\}$ into $\hat{y} \in \mathbb{R}^{64}$	3×3 ConvSN, $1 \rightarrow 128$
Concatenate z and \hat{y} into $h \in \mathbb{R}^{128}$	LeakyReLU, Avg. Pool
Project and reshape h to $7 \times 7 \times 128$	3×3 ConvSN, $128 \rightarrow 256$
3×3 ConvSN, $128 \rightarrow 512$	LeakyReLU, Avg. Pool
ReLU; Up $2 \times$	3×3 ConvSN, $256 \rightarrow 512$
3×3 ConvSN, $512 \rightarrow 256$	LeakyReLU, Avg. Pool
CCBN(\cdot, h); ReLU; Up $2 \times$	Global Average Pool into f
3×3 ConvSN, $256 \rightarrow 128$	Embed $y \in \{0, \dots, 9\}$ into \hat{y}'
CCBN(\cdot, h); ReLU	Projection step(\hat{y}', f)
3×3 ConvSN, $128 \rightarrow 1$	
tanh()	

Table 3. Architectures used for the standard generator and discriminator in the Rotated MNIST experiments.

Generator	Discriminator
Sample $z \in \mathbb{R}^{64} \sim \mathcal{N}(0, I)$	Input RGB image $x \in \mathbb{R}^{28 \times 28 \times 1}$
Embed $y \in \{0, \dots, 9\}$ into $\hat{y} \in \mathbb{R}^{64}$	3×3 $z2 - p4$ GConvSN, $1 \rightarrow 64$
Concatenate z and \hat{y} into $h \in \mathbb{R}^{128}$	LeakyReLU, Avg. Pool
Project and reshape h to $7 \times 7 \times 128$	3×3 $p4 - p4$ GConvSN, $64 \rightarrow 128$
3×3 $z2 - p4$ GConvSN, $128 \rightarrow 256$	LeakyReLU, Avg. Pool
ReLU; Up $2 \times$	3×3 $p4 - p4$ GConvSN, $128 \rightarrow 256$
3×3 $p4 - p4$ GConvSN, $256 \rightarrow 128$	LeakyReLU, Avg. Pool
CCBN(\cdot, h); ReLU; Up $2 \times$	$p4$ -Max Pool
3×3 $p4 - p4$ GConvSN, $128 \rightarrow 64$	Global Average Pool into f
CCBN(\cdot, h); ReLU	Embed $y \in \{0, \dots, 9\}$ into \hat{y}'
3×3 $p4 - p4$ GConvSN, $64 \rightarrow 1$	Projection step(\hat{y}', f)
$p4$ -Max Pool	
tanh()	

Table 4. Architectures used for the $p4$ -equivariant generator and discriminator in the Rotated MNIST experiments.

Generator	Discriminator
Sample $z \in \mathbb{R}^{128} \sim \mathcal{N}(0, I)$	Input RGB image $x \in \mathbb{R}^{128 \times 128 \times 3}$
Embed $y \in \{0, \dots, 4\}$ into $\hat{y} \in \mathbb{R}^{128}$	$z2 - z2$ ResBlockD, $3 \rightarrow 32$
Concatenate z and \hat{y} into $h \in \mathbb{R}^{256}$	$z2 - z2$ ResBlockD, $32 \rightarrow 64$
Project and reshape h to $4 \times 4 \times 128$	$z2 - z2$ ResBlockD, $64 \rightarrow 128$
$z2 - z2$ ResBlockG, $128 \rightarrow 512$	$z2 - z2$ ResBlockD, $128 \rightarrow 256$
$z2 - z2$ ResBlockG, $512 \rightarrow 256$	$z2 - z2$ ResBlockD, $256 \rightarrow 512$
$z2 - z2$ ResBlockG, $256 \rightarrow 128$	ReLU
$z2 - z2$ ResBlockG, $128 \rightarrow 64$	Global Average Pool into f
$z2 - z2$ ResBlockG, $64 \rightarrow 32$	Embed $y \in \{0, \dots, 4\}$ into \hat{y}'
BN; ReLU	Projection step(\hat{y}', f)
3×3 ConvSN, $32 \rightarrow 3$	
$\tanh()$	

Table 5. Architectures used for the standard generator and discriminator in the ANHIR experiments.

Generator	Discriminator
Sample $z \in \mathbb{R}^{128} \sim \mathcal{N}(0, I)$	Input RGB image $x \in \mathbb{R}^{128 \times 128 \times 3}$
Embed $y \in \{0, \dots, 4\}$ into $\hat{y} \in \mathbb{R}^{128}$	$z2 - p4m$ ResBlockD, $3 \rightarrow 11$
Concatenate z and \hat{y} into $h \in \mathbb{R}^{256}$	$p4m - p4m$ ResBlockD, $11 \rightarrow 22$
Project and reshape h to $4 \times 4 \times 128$	$p4m - p4m$ ResBlockD, $22 \rightarrow 45$
$z2 - p4m$ ResBlockG, $128 \rightarrow 181$	$p4m - p4m$ ResBlockD, $45 \rightarrow 90$
$p4m - p4m$ ResBlockG, $181 \rightarrow 90$	$p4m - p4m$ ResBlockD, $90 \rightarrow 181$
$p4m - p4m$ ResBlockG, $90 \rightarrow 45$	ReLU
$p4m - p4m$ ResBlockG, $45 \rightarrow 22$	$p4m$ -Max Pool
$p4m - p4m$ ResBlockG, $22 \rightarrow 11$	Global Average Pool into f
$p4m$ -BN; ReLU	Embed $y \in \{0, \dots, 4\}$ into \hat{y}'
3×3 $p4m - p4m$ GConvSN, $11 \rightarrow 3$	Projection step(\hat{y}', f)
$p4m$ -Max Pool	
$\tanh()$	

Table 6. Architectures used for the $p4m$ -equivariant generator and discriminator in the ANHIR experiments.

Generator	Discriminator
Sample $z \in \mathbb{R}^{128} \sim \mathcal{N}(0, I)$	Input RGB image $x \in \mathbb{R}^{256 \times 256 \times 3}$
Embed $y \in \{0, 1, 2\}$ into $\hat{y} \in \mathbb{R}^{128}$	$z2 - z2$ ResBlockD-BN, 3 \rightarrow 16
Concatenate z and \hat{y} into $h \in \mathbb{R}^{256}$	$z2 - z2$ ResBlockD-BN, 16 \rightarrow 32
Project and reshape h to $4 \times 4 \times 128$	$z2 - z2$ ResBlockD-BN, 32 \rightarrow 64
$z2 - z2$ ResBlockG, 128 \rightarrow 512	$z2 - z2$ ResBlockD-BN, 64 \rightarrow 128
$z2 - z2$ ResBlockG, 512 \rightarrow 256	$z2 - z2$ ResBlockD-BN, 128 \rightarrow 256
$z2 - z2$ ResBlockG, 256 \rightarrow 128	$z2 - z2$ ResBlockD-BN, 256 \rightarrow 512
$z2 - z2$ ResBlockG, 128 \rightarrow 64	ReLU
$z2 - z2$ ResBlockG, 64 \rightarrow 32	Global Average Pool into f
$z2 - z2$ ResBlockG, 32 \rightarrow 16	Embed $y \in \{0, 1, 2\}$ into \hat{y}'
BN; ReLU	Projection step(\hat{y}', f)
3×3 ConvSN, 16 \rightarrow 3	
$\tanh()$	

Table 7. Architectures used for the standard generator and discriminator in the LYSTO experiments.

Generator	Discriminator
Sample $z \in \mathbb{R}^{128} \sim \mathcal{N}(0, I)$	Input RGB image $x \in \mathbb{R}^{256 \times 256 \times 3}$
Embed $y \in \{0, 1, 2\}$ into $\hat{y} \in \mathbb{R}^{128}$	$z2 - p4m$ ResBlockD-BN, 3 \rightarrow 5
Concatenate z and \hat{y} into $h \in \mathbb{R}^{256}$	$p4m - p4m$ ResBlockD-BN, 5 \rightarrow 11
Project and reshape h to $4 \times 4 \times 128$	$p4m - p4m$ ResBlockD-BN, 11 \rightarrow 22
$z2 - p4m$ ResBlockG, 128 \rightarrow 181	$p4m - p4m$ ResBlockD-BN, 22 \rightarrow 45
$p4m - p4m$ ResBlockG, 181 \rightarrow 90	$p4m - p4m$ ResBlockD-BN, 45 \rightarrow 90
$p4m - p4m$ ResBlockG, 90 \rightarrow 45	$p4m - p4m$ ResBlockD-BN, 90 \rightarrow 181
$p4m - p4m$ ResBlockG, 45 \rightarrow 22	ReLU
$p4m - p4m$ ResBlockG, 22 \rightarrow 11	$p4m$ -Max Pool
$p4m - p4m$ ResBlockG, 11 \rightarrow 5	Global Average Pool into f
$p4m$ -BN; ReLU	Embed $y \in \{0, 1, 2\}$ into \hat{y}'
3×3 $p4m - p4m$ GConvSN, 5 \rightarrow 3	Projection step(\hat{y}', f)
$p4m$ -Max Pool	
$\tanh()$	

Table 8. Architectures used for the $p4m$ -equivariant generator and discriminator in the LYSTO experiments.

Generator	Discriminator
Sample $z \in \mathbb{R}^{64} \sim \mathcal{N}(0, I)$	Input RGB image $x \in \mathbb{R}^{64 \times 64 \times 3}$
Embed $y \in \{0, \dots, 100\}$ into $\hat{y} \in \mathbb{R}^{64}$	$z2 - z2$ ResBlockD, 3 \rightarrow 128
Concatenate z and \hat{y} into $h \in \mathbb{R}^{128}$	$z2 - z2$ ResBlockD, 128 \rightarrow 256
Project and reshape h to $4 \times 4 \times 1024$	$z2 - z2$ ResBlockD, 256 \rightarrow 512
$z2 - z2$ ResBlockG, 1024 \rightarrow 512	$z2 - z2$ ResBlockD, 512 \rightarrow 784
$z2 - z2$ ResBlockG, 512 \rightarrow 384	ReLU
$z2 - z2$ ResBlockG, 384 \rightarrow 256	Global Average Pool into f
$z2 - z2$ ResBlockG, 256 \rightarrow 192	Embed $y \in \{0, \dots, 100\}$ into \hat{y}'
BN; ReLU	Projection step(\hat{y}', f)
3×3 ConvSN, 192 \rightarrow 3	
tanh()	

Table 9. Architectures used for the standard generator and discriminator in the Food-101 experiments.

Generator	Discriminator
Sample $z \in \mathbb{R}^{64} \sim \mathcal{N}(0, I)$	Input RGB image $x \in \mathbb{R}^{64 \times 64 \times 3}$
Embed $y \in \{0, \dots, 100\}$ into $\hat{y} \in \mathbb{R}^{64}$	$z2 - p4$ ResBlockD, 3 \rightarrow 64
Concatenate z and \hat{y} into $h \in \mathbb{R}^{128}$	$p4 - p4$ ResBlockD, 64 \rightarrow 128
Project and reshape h to $4 \times 4 \times 1024$	$p4 - p4$ ResBlockD, 128 \rightarrow 256
$z2 - p4$ ResBlockG, 1024 \rightarrow 256	$p4 - p4$ ResBlockD, 256 \rightarrow 392
$p4 - p4$ ResBlockG, 256 \rightarrow 192	ReLU
$p4 - p4$ ResBlockG, 192 \rightarrow 128	$p4$ -Max Pool
$p4 - p4$ ResBlockG, 128 \rightarrow 96	Global Average Pool into f
$p4$ -BN; ReLU	Embed $y \in \{0, \dots, 100\}$ into \hat{y}'
3×3 $p4 - p4$ GConvSN, 96 \rightarrow 3	Projection step(\hat{y}', f)
$p4$ -Max Pool	
tanh()	

Table 10. Architectures used for the $p4$ -equivariant generator and discriminator in the Food-101 experiments.

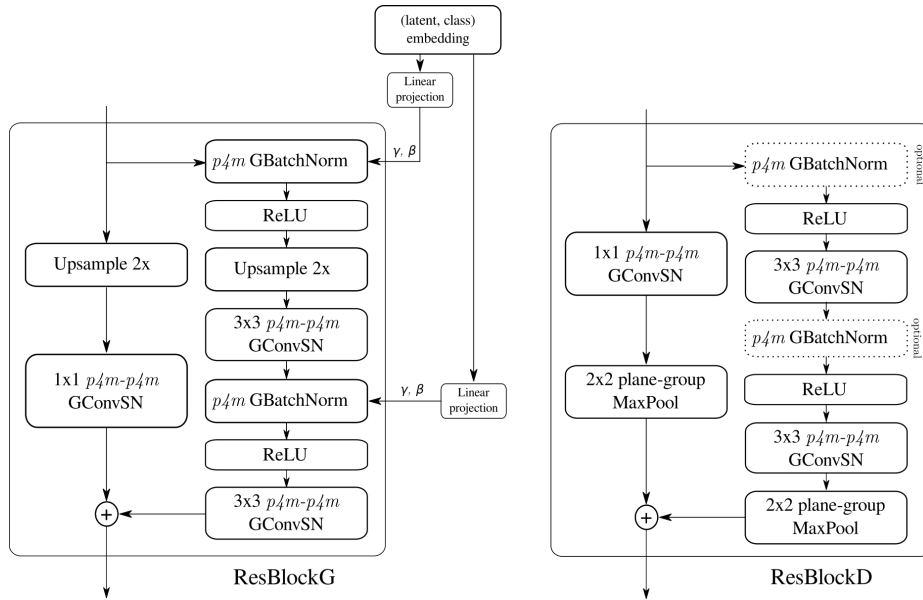


Fig. 15. Residual blocks in the group-equivariant settings used in RGB image generation architectures. The choice of p_4 or p_{4m} is dataset-specific. The generator uses ResBlockG (left) and the discriminator uses ResBlockD (right). The first residual block in the convolutional sequence in either network uses z_2 - p_{4m} group-convolutions for the initial layer. The non-equivariant settings replace all group-convolutions and normalizations within the residual blocks with standard techniques. Visual design inspired by [9].